nature communications

Article

https://doi.org/10.1038/s41467-024-53924-9

High-performance photon-driven DC motor system

Received: 2 April 2024

Accepted: 28 October 2024

Published online: 04 November 2024

Check for updates

Dingyi Lin[1], Fujin Deng[1] ✉, Wei Hua[1], Ming Cheng[1], Zhe Chen[2] & Zhiming Wang[3]

Direct current (DC) motors are crucial in drones, robotics, and electrical devices. Conventionally, the DC motor is driven by a switching electricity converter, which utilizes electrical energy to drive mechanical motion. However, the rapid on-off switching actions in the switching electricity converter would cause electromagnetic interference (EMI), impairing the functionality of drive systems. Here, we propose a photon-driven DC motor system based on photonic converter, which utilizes optical energy to drive mechanical motion, and therefore avoids EMI derived from electrical switching and immunizes against EMI during electrical energy transmission in conventional switching electricity-driven DC motor system. The operation principle and power modulation-based speed control are also presented for the proposed photon-driven DC motor system. The experiments demonstrate that the motor accurately follows the speed reference and withstands load disturbances. This innovation opens new potential for DC motor applications by improving electromagnetic compatibility.

Direct current (DC) motor plays a critical role in drones, robotics, and electrical devices[1–3]. The brushed DC motor, which is the most widely used DC motor, employs brushes to conduct DC electricity to the rotating part of the motor (the armature). This process continuously changes the flow of electricity that generates mechanical motion. The brushed DC motor is an attractive option in various applications because of its simple design, wide availability, easy control, and good reliability.

A conventional brushed DC motor drive system is illustrated in Fig. 1a, which is known as a switching electricity converter-driven DC motor system. The switching electricity converter is employed to convert the DC electricity power to drive the DC motor, where a controller is adopted for the switching electricity converter to regulate the DC motor's speed based on its received feedback signals from motor sensors via electricity wires. In Fig. 1a, the excepted output voltage V_{out} of the switching electricity converter is modulated by the switching electricity converter through periodical on-off switching actions of the power semiconductor switches. However, the rapid on-off switching actions generate high-frequency electromagnetic waves[4–9], and causes intrinsic electromagnetic interference (EMI), which would adversely affect nearby electronic devices by inducing unwanted currents and voltages. Besides, the rapid on-off switching actions in the switching electricity converter also inherently cause ripple of its output voltage V_{out}[10], which would lead to torque ripple of the motor, and thereby increasing the difficulty of motor control[11]. On the other hand, the environmental EMI[12–16], common in industrial environments, would introduce noise into feedback and control signals of the switching electricity converter, which would also increase difficulty of motor control. To protect against EMI and ensure high-performance motor control, effective EMI impact elimination is crucial.

Light, as an alternative energy carrier, presents an innovative approach to overcome EMI challenges. The power over fiber (PoF)[17–23] employs fibers to transmit optical energy, which can overcome EMI issues inherent in electrical energy transmission. In the PoF, continuous monochromatic light from a laser is transmitted via optical fibers, and converted into electricity by photovoltaic devices. Compared to traditional electrical energy transmission by metal wire, the

[1]School of Electrical Engineering, Southeast University, Nanjing, China. [2]Department of Energy Technology, Aalborg University, Aalborg, Denmark. [3]Institute of Fundamental and Frontier Sciences, University of Electronic Science and Technology of China, Chengdu, China. ✉e-mail: fdeng@seu.edu.cn

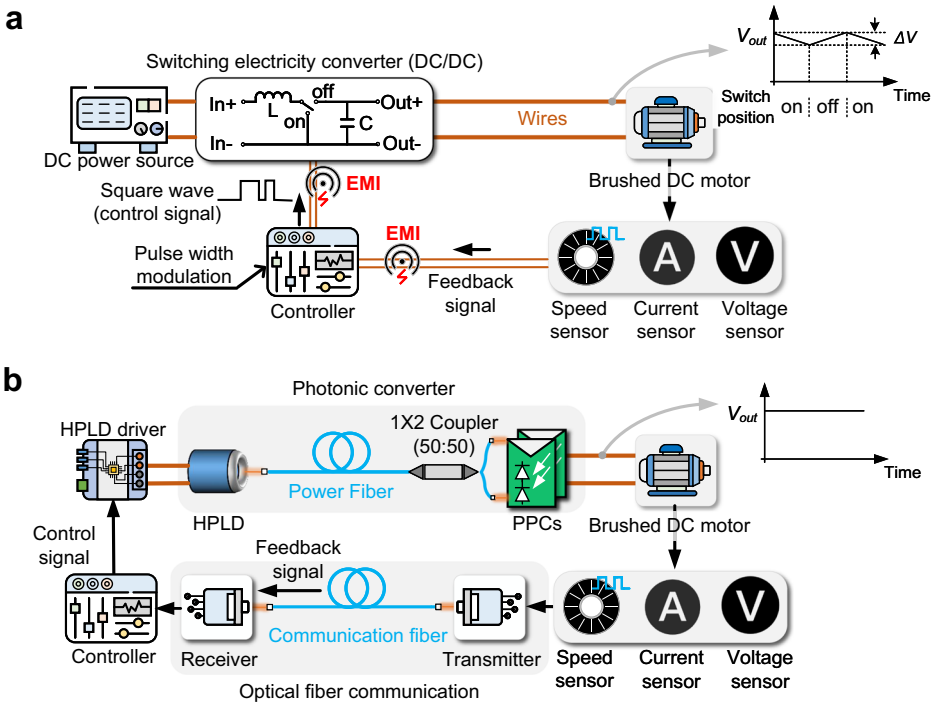

Fig. 1 | Schematic of a switching electricity-driven DC motor system and proposed photon-driven DC motor system. a Schematic of a conventional switching electricity-driven DC motor system, equipped with a switching electricity converter (boost converter), exhibits its steady-state output voltage over time under the linear-ripple approximation. EMI electromagnetic interference, DC direct current. V_{out} the output voltage of the switching electricity converter. ΔV output voltage ripple magnitude. **b** Schematic of a photon-driven DC motor system, showing its steady-state output voltage over time, characterized by an approximately ripple-free condition. HPLD high-power laser diode, PPC photovoltaic power converter.

PoF offers immunity to EMI due to the non-conductive nature of optical fibers[19–21]. This makes them ideal for use in environments with high levels of EMI. Furthermore, PoF ensures galvanic isolation, weight reduction, and eliminates the risk of fire or electrical shock in metal wires[19–21]. To eliminate the impact of EMI on conventional DC motor drive system, PoF is an attractive solution.

In this work, a photon-driven DC motor system is proposed, which integrates PoF and DC motor control, and employs optical energy to regulate DC motor's speed, as shown in Fig. 1b. In the proposed system, a photonic converter is utilized to regulate the DC motor's speed, which is controlled by the laser driver. Here, the optical power of the high-power laser diode (HPLD) is controlled by the laser driver to regulate the DC motor's speed by the controller based on its receiving feedback signals from the motor sensors via optical fiber communication. In the photonic converter, the HPLD is used to convert electrical energy into optical energy, which is transmitted through optical fiber and fiber coupler. And then, the photovoltaic power converters[24–31] (PPCs) are used to convert optical energy back into electrical energy for the motor. Owing to the optical power is continuously controlled in the photonic converter, the photon-driven motor system can significantly eliminate intrinsic EMI and voltage ripple in the conventional switching electricity-driven motor system. Owing to adoption of photonic converter and fibers, the photon-driven motor system is immune to the environment EMI. In this work, the HPLD-PPC-Motor model for the proposed photon-driven DC motor system is analyzed, proposing an operation principle and a power modulation (PM)-based speed control, due to the incompatibility between conventional switching electricity converter-based control and the photon-driven DC motor system.

An experimental prototype with off-the-shelf discrete components is constructed and three situations are conducted: (1) braking and starting under constant load, (2) tracking a sinusoidal speed reference with constant load, and (3) tracking constant speed with load disturbance. Experiment results show that the proposed system can effectively track the speed reference and can resist load disturbance. Besides, the measurement results demonstrate that the intensity of electromagnetic field emission from the photonic converter is at an environmental level and lower than that of the switching electricity converter across a broad frequency range. Furthermore, the measurement results demonstrate that the photonic converter has the rejection of output voltage ripple.

The photon-driven DC motor system presents a revolutionary approach in high-level environmental EMI applications, such as a mobile tethered unmanned aerial vehicle (tUAV) for monitoring high voltage transmission lines and an auxiliary motor drive system of electromagnetic catapult system. For example, the conventional tUAV connects to a mobile ground station (GS) via a metal wire tether, which supplies power to the tUAV, as shown in Fig. 2a, where the metal wires are susceptible to EMI, impairing the functionality of the supply power. Besides, the weight of the metal wire limits tethering distances to ~150 m[32–34]. To address EMI challenge and extend the tethering distance in conventional tUAV, the photon-driven DC motor system can be employed in the tUAV, where the HPLD in the GS is connected to the PPCs in the tUAV through the fiber, as shown in Fig. 2b, c. Since fiber is immune to environmental EMI and lighter than wire, it enables the potential for EMI resistance and longer tethering distances, overcoming previous limitations and opening new possibilities for tUAV applications.

Results

Photon-driven DC motor system structure

The proposed photon-driven DC motor system is shown in Fig. 1b. The DC motor speed is regulated by the photonic converter, which is controlled by the controller via a HPLD driver. The optical fiber communication is used to transmit the feedback signals from sensors, such as motor speed, to the controller. In the proposed photon-

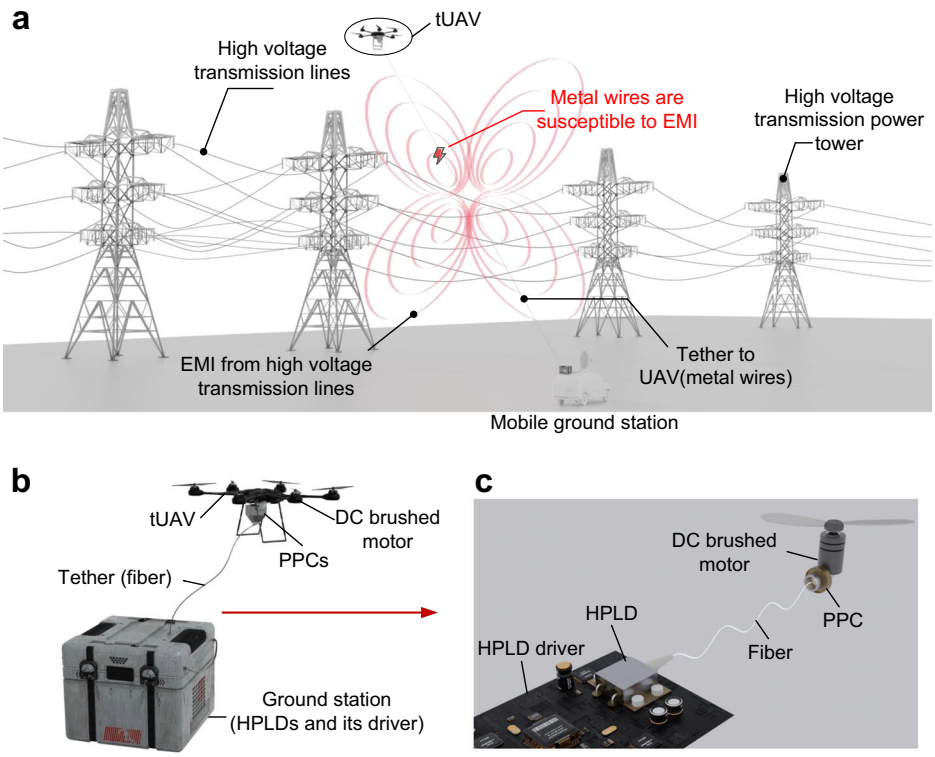

Fig. 2 | Schematic of tUAV application and its basic structure. a Schematic of a mobile tUAV for monitoring high voltage transmission lines. tUAV tethered unmanned aerial vehicle. **b** The photon-driven DC motor system is applied to the propeller motors of the tUAV. **c** Partial schematic diagram of photon-driven DC motor system in the tUAV.

driven DC motor system, the photonic converter is mainly comprised of HPLD, fiber, and PPC. The HPLD is utilized to continuously supply optical power to the PPC via a fiber. The PPC is utilized to convert the optical power into suitable electrical power for driving DC motor. Supplementary Fig. 1 provides a comparison of the energy conversion process between the proposed system and the conventional system.

Theoretical analysis of HPLD-PPC-Motor model

A HPLD-PPC-Motor model based on the theoretical equivalent circuit model, as shown in Fig. 3a and b, is proposed to derive the theoretical performance of the proposed system. This model involves the photoelectric characteristics of the HPLD and PPC, as well as the electrical and mechanical characteristics of the DC motor. The HPLD model is the electro-optic equivalent circuit[35,36], and the HPLD requires to operate in its linear interval (the gray area in Supplementary Fig. 2). In this linear interval, the injection current of the HPLD I_{HPLD} is linear to the output optical power P_{light_HPLD} of the HPLD, i.e., $P_{light\_HPLD} \propto I_{HPLD}$. Thus, the P_{light_HPLD} can be modulated by the I_{HPLD} (see section "Method" for the details).

The fiber model shows the output optical power P_{light_HPLD} of the HPLD is linear to the input optical power P_{light_PPC} of the PPC, i.e., $P_{light\_PPC} \propto P_{light\_HPLD}$ in the optical energy transmission from HPLD to PPC via the fiber. The model of the fiber is based on the Bouguer-Beer-Lambert law[37,38], which shows that the power of light in optical energy transmission by the fiber is exponential attenuation over distance. This attenuation, caused primarily by absorption and scattering in the fiber, is quantified as attenuation coefficient α in decibels per kilometer (dB/km). The α depends on two factors, including the distance of light propagation and the light's wavelength. For a wavelength of 808 nm, the α is around 2.0 dB/km. For the wavelength of 975 nm, the α is around 0.8 dB/km[39]. The α for SiO_2 fiber is shown in Supplementary Fig. 3 under different wavelengths and distances from 0 m to 1 km. For a specific fiber, the distance of light propagation and wavelength are constant, that is, the α for this fiber is also constant. Therefore, $P_{light\_PPC} \propto P_{light\_HPLD}$ (see section "Method" for the details). Moreover, HPLD and PPC efficiencies vary by wavelength: 808 nm HPLDs have an over 45% efficiency[25,40], while 975 nm reach over 50%[41]. PPCs operate at over 55% efficiency[42] for 800–850 nm and over 24%[20,43] for 900–980 nm. This study selects the 808 nm wavelength for high PPC efficiency.

The PPC model is the single diode equivalent circuit[44,45](see section "Method" for details), which consists of a series resistor, a parallel resistor, a diode, and a current source, as shown in Fig. 3a. The PPC receives input optical power P_{light_PPC}, and generates photogenerated current I_{ph} of the PPC, which determines the output current I_{ppc} of the PPC and the output voltage V_{ppc} through the load characteristics. Figure 3c, d show the current–voltage (I_{ppc}–V_{ppc}) and power–voltage (P_{ppc}–V_{ppc}) curves of the PPC employed in this study with P_{light_PPC} from 1.5 W to 6 W. Figure 3e shows the curves between the I_{ph} and the P_{light_PPC}, where $I_{ph} \propto P_{light\_PPC}$. Here, $P_{ppc} = V_{ppc} \cdot I_{ppc}$. In Fig. 3c, d, the maximum power points (MPP) are the maximum electrical power output corresponding to various P_{light_PPC}, which are located at the "knee" regions of the $I_{ppc} - V_{ppc}$ curve. To the left of the MPP, the I_{ppc} is approximately equal to the I_{ph}, i.e., $I_{ppc} \approx I_{ph}$. To the right of the MPP, I_{ppc} drops sharply as the V_{ppc} increases.

The brushed DC motor model[1] is shown in Fig. 3a, which is composed of armature winding inductance L_a, armature winding resistance R_a, and the back electromotive force (EMF) e (see section "Method" for details). The DC motor receives armature current I_a, and generates electromagnetic torque T_e. The motor speed ω_{rm} is determined when the T_e balances with the load torque T_L. An increase in the I_a results in greater T_e, which leads to an increase in ω_{rm} under the same T_L. Figure 3c, d show the I_a–V_{ppc} curves and the P_a–V_{ppc} curves of the DC motor used in this work, respectively, under different T_L from 20–40 mNm, where the input power $P_a = V_{ppc} \cdot I_a$.

https://doi.org/10.1038/s41467-024-53924-9

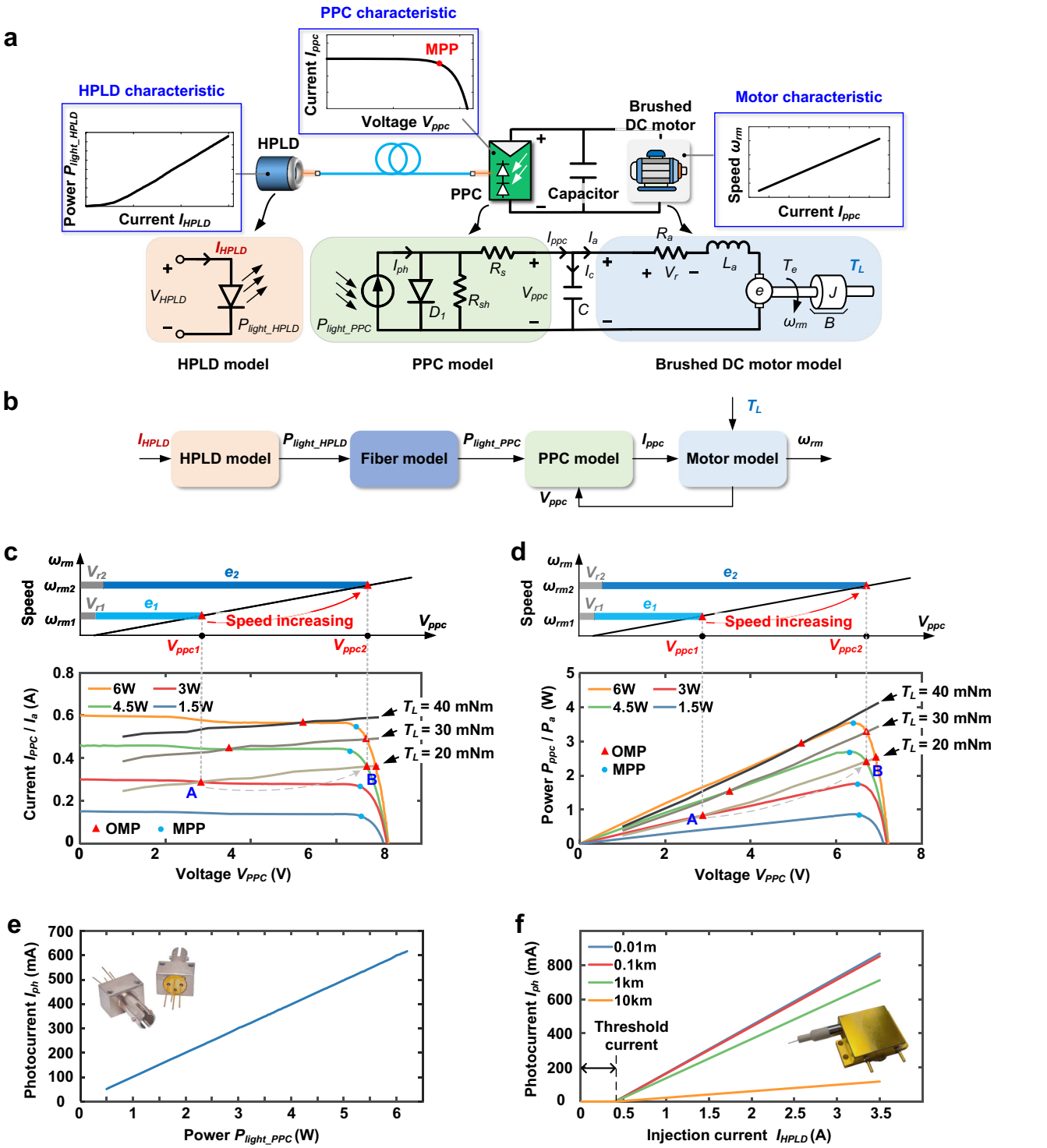

Fig. 3 | Schematic of the operation principle of the photonic converter. a The equivalent circuit of the HPLD-PPC-Motor model. The output current (I_{ppc}) and output voltage (V_{ppc}) of the PPC are equal to the armature current (I_a) and the terminal voltage (V_{ppc}) of the brushed DC motor, respectively. I_{ph} denotes photo-generated current of the PPC, D_1 denotes p–n junction diode, R_{sh} denotes shunt resistance, R_s denotes series resistance, C denotes shunt capacitance, I_c denotes capacitance current, R_a denotes armature winding resistance, L_a denotes armature winding inductance, e denotes back electromotive force (EMF), T_e and T_L denote the electromagnetic torque and load torque, respectively. ω_{rm} is the rotating angular speed of the rotor, J is the inertia coefficient, and B is the viscous damping coefficient. MPP, maximum power point. **b** The relationship between different models within the HPLD-PPC motor model. **c** Current–voltage (I_{ppc}–V_{ppc}) curves for the PPC at the input optical power of 1.5, 3, 4.5, and 6 W with current–voltage (I_a–V_{ppc}) curves for the brushed DC motor at load torque of 20, 30, and 40 mNm. OMP operational matching point. **d** Power–voltage (P_{ppc}–V_{ppc}) curves for the PPC at the optical power of 1.5, 3, 4.5, and 6 W with power–voltage (P_a–V_{ppc}) curves for the brushed DC motor at the load torque of 20, 30, and 40 mNm. **e** Photocurrent–input optical power (I_{ph}–P_{light_PPC}) curve for the PPC. **f** Photocurrent–injection current (I_{ph}–I_{HPLD}) curves for the photonic converter under fiber transmission distance from 10 m to 10 km. The used parameters are listed in Supplementary Table 1 and Supplementary Table 2.

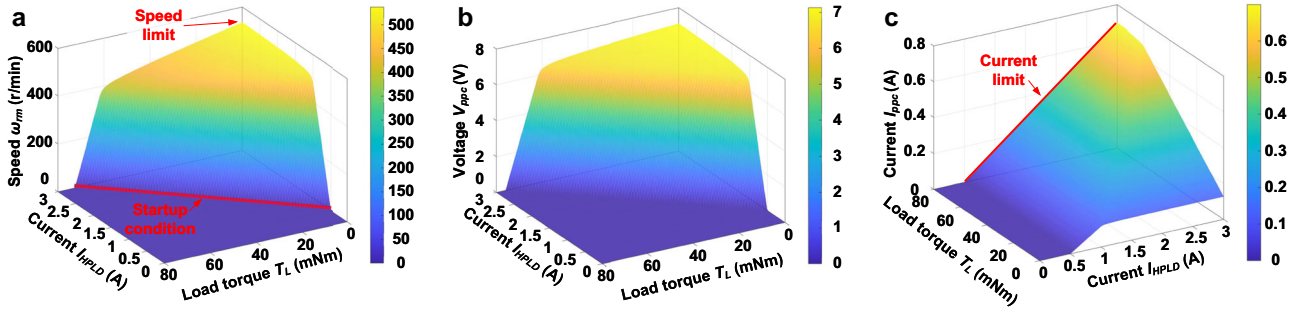

Fig. 4 | Theoretical model performance of the proposed photonic converter. **a** The speed-load torque-current of the HPLD(ω_{rm}–T_L–I_{HPLD}) relationship of the photonic converter for DC motor. The depicted red line signifies the startup conditions, where the electromagnetic torque surpasses the T_L, thereby the motor starts rotating. **b** The voltage of the PPC-load torque-current of the HPLD (V_{ppc}–T_L–I_{HPLD}) relationship of the photonic converter for DC motor. **c** The current of the PPC-load torque-current of the HPLD (I_{ppc}–T_L–I_{HPLD}) relationship of the photonic converter for DC motor. The used parameters are listed in Supplementary Table 1 and Supplementary Table 2.

The HPLD-PPC-Motor model of the proposed photon-driven DC motor system can be obtained by combing models of HPLD, fiber, PPC and DC motor. The I_{HPLD} determines the P_{light_HPLD}, P_{light_PPC}, and I_{ph} (Fig. 3f shows the I_{ph}–I_{HPLD} curves with fiber distances from 0.01 km to 10 km), which determines the I_{ppc}. I_c is capacitor current and $I_{ppc} = I_a + I_c$. Given the T_L, the I_a determines the T_e, which further determines the ω_{rm}. Therefore, the motor speed ω_{rm} as a function of I_{HPLD} and T_L can be written as

$$\omega_{rm} = \frac{K_t}{B}\left[R_{HPLD}\eta_{trans}R_{PPC}\left(I_{HPLD} - I_{th}\right)\right] - \frac{K_t I_o}{B}\left[\exp\left(\frac{A_1}{nV_T}\right) - 1\right] - \frac{K_t A_1}{BR_{sh}} - \frac{K_t I_c}{B} - \frac{T_L}{B} - \frac{J}{B}\frac{d\omega_{rm}}{dt} \quad (1)$$

with

$$A_1 = \frac{B\omega_{rm} + T_L + J\frac{d\omega_{rm}}{dt}}{K_t}R_a + K_e\omega_{rm} + \left(\frac{B\omega_{rm} + T_L + J\frac{d\omega_{rm}}{dt}}{K_t} + I_c\right)R_s + L_a\frac{d\left(B\omega_{rm} + T_L + J\frac{d\omega_{rm}}{dt}\right)}{dt} \quad (2)$$

where K_t is torque constant, B is viscous damping coefficient, R_{HPLD} is differential slope efficiency, η_{trans} is power efficiency, R_{PPC} is differential responsivity, I_{th} is threshold current, I_o is diode reverse saturation current, n is diode ideality constant, V_T is junction thermal voltage, R_{sh} is shunt resistance of the PPC, and R_s is series resistance of the PPC, J is inertia coefficient (see Method for the function derivation).

In the HPLD-PPC-Motor model as shown in Fig. 4a, given the load torque T_L, the ω_{rm} can be controlled by the P_{light_PPC}, which is regulated by the I_{HPLD}. Figure 4a shows the ω_{rm} as a function of I_{HPLD} and T_L based on the PPC and DC motor parameters used in this work, where a distinct red line highlights a startup condition of the motor. Figure 4b shows the V_{ppc} as a function of I_{HPLD} and T_L. Figure 4c shows the I_{ppc} as a function of I_{HPLD} and T_L. The same trend between ω_{rm} and V_{ppc} can be observed within Fig. 4a, b. Here, V_{ppc} cannot surpass the open-circuit voltage of the PPC and the I_{ppc} cannot exceed I_{ph}, as shown in Fig. 4b, c, thereby limiting the increase of V_{ppc} and ω_{rm}. Supplementary Fig. 4 presents a comparison between the theoretical model and experimental data, including ω_{rm}, V_{ppc}, and I_{ppc}. It is worth mentioning that the photon-driven DC motor system has an anti-disturbance capability to the fluctuations of load torque T_L, which is not available in switching electricity converter-driven DC motor system (see Supplementary Note 1 for the principle of anti-disturbance capability).

Operation principle of photon-driven DC motor

The operation principle of the proposed photon-driven DC motor is proposed based on aforementioned HPLD-PPC-Motor model, where the photon-driven DC motor works at the corresponding operational matching point (OMP) in the steady state under different P_{light_PPC} (i.e., different I_{HPLD}) and different T_L, as shown in Fig. 3c, d. The OMPs are the intersections (red triangles) of the PPC's I_{ppc}–V_{ppc} curves and the DC motor's I_a–V_{ppc} curves, where there is $I_{ppc} = I_a$ in the OMP in the steady state. For an example, suppose that the photon-driven DC motor works at OMP A ($P_{light\_PPC} = 3$ W, i.e., $I_{HPLD} \approx 1.48$ A under 10 m fiber, and $T_L = 20$ mNm), an increase of the P_{light_PPC} to 4.5 W, i.e., $I_{HPLD} \approx 2.01$ A under 10 m fiber, would lead to change in the PPC's voltage and current curves (approximate curve shifts upward), which leads to a rise in current (I_{ppc} and I_a), voltage V_{ppc}, and speed ω_{rm}, and finally works at OMP B steadily. Figure 3c shows that as the T_L increases, to remain same ω_{rm}, the P_{light_PPC} needs to be increased. If the T_L remains unchanged, to increase the ω_{rm}, the P_{light_PPC} needs to be increased.

Power modulation-based speed control

An innovative power modulation (PM)-based speed control for the proposed photon-driven DC motor system is proposed based on aforementioned HPLD-PPC-Motor model and proposed operation principle, as shown in Fig. 5a. The PM-based speed control is composed of the controller, the photonic converter, optical fiber communication, and a suite of sensors. In the PM-based speed control, the control structure includes the system model (Fig. 5b) and the control scheme (Fig. 5c). The proportional-integral (PI) controller is used in this paper, which is renowned for efficacy in error correction and system stability enhancement. The operational flow begins with acquiring real-time feedback signals, including the ω_{rm} and V_{ppc} obtained from these sensors. These signals are then sent to the controller via optical fiber communication, marking the initiation of the speed control process. The control scheme is achieved by computing the speed error, which is the difference between the speed reference ω_{ref} and the ω_{rm}. Based on the speed error, the PI controller control the reference of I_{HPLD}, which is subsequently sent to the HPLD driver, and then control the HPLD's output optical power P_{light_HPLD} and the ω_{rm}. The control design for the proposed system is shown in the Supplementary Note 2. Since specific scenarios require the motor to have forward and reverse rotation functions, a topology that can realize forward and reverse rotation functions based on the photonic converter is proposed to meet this requirement, see Supplementary Note 3 for details.

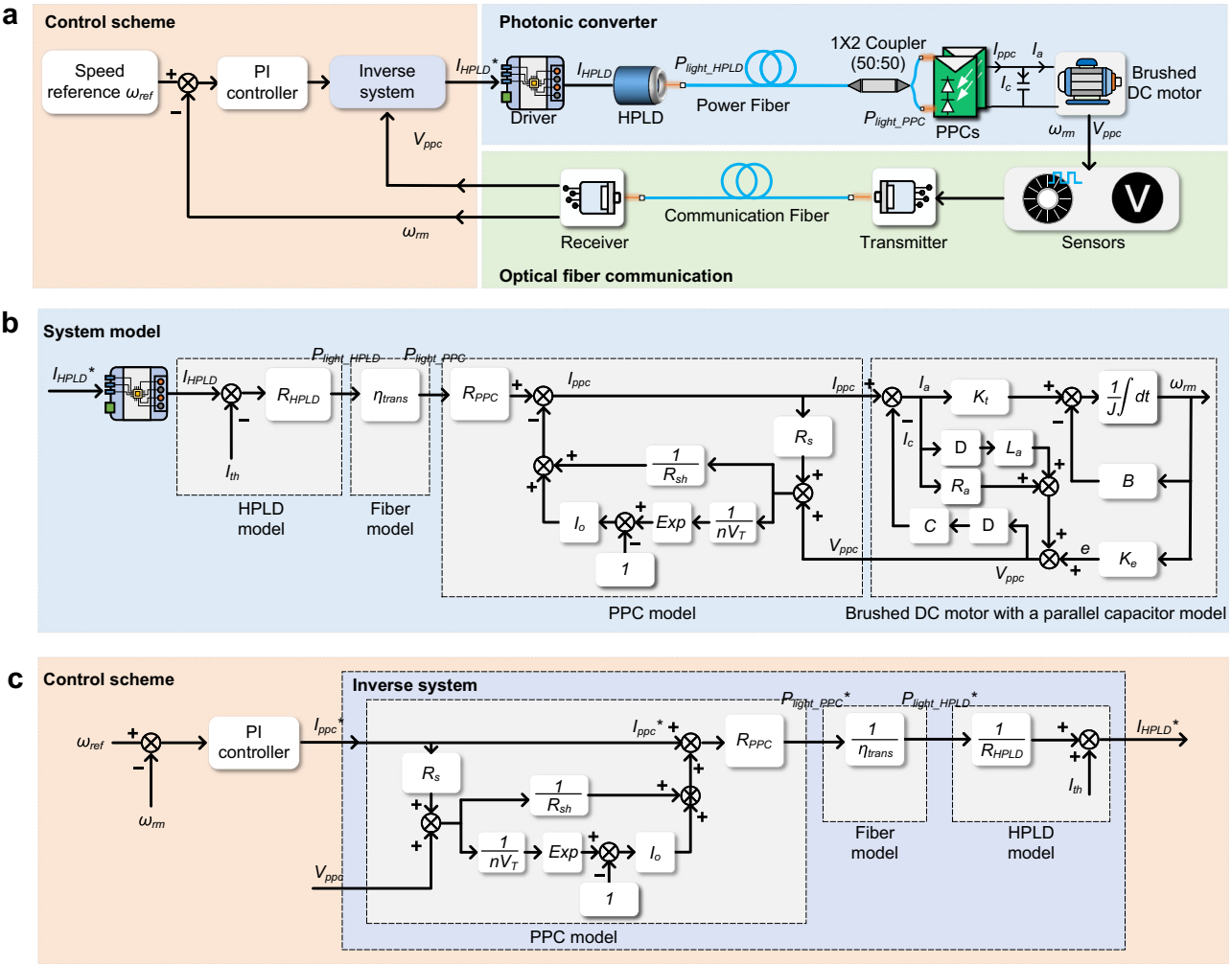

Fig. 5 | Schematic of the proposed PM-based speed control for the photon-driven DC motor system. a The control structure of the PM-based speed control in the photonic converter and experimental setup. **b** The system model of the photonic converter. **c** Control scheme of the proposed system. The speed reference is the input variable and the injection current reference of the HPLD is the output variable.

Experimental verification of PM-based speed control

A prototype was constructed to verify the PM-based speed control of the photon-driven DC motor system, and its performance was tested using commercially available off-the-shelf components including an HPLD driver, HPLD, PPC, and a brushed DC motor. The experimental setup is shown in Fig. 5a, and its photos are shown in Fig. 6a (see section "Methods" for the construction of photonic converter prototype, Supplementary Fig. 5 for experimental results in the oscilloscope display diagram, and Supplementary Fig. 6 for the relationship between the brake injection current I_{torque} and output load torque T_L). To prove that the proposed system can achieve speed control, three test situations are designed to verify the efficiency and feasibility of the motor system. The first test situation is that the DC motor brakes and starts under constant load torque. The second test situation is that the DC motor follows a sinusoidally varying speed reference command with constant load torque. The third test situation is that the DC motor tracks the constant speed reference command with load disturbance.

Test situation 1: braking and starting under constant load. Figure 6b, c shows the experimental result of the first test situation, where the dynamic response of a DC motor under variable control commands is observed. Initially, the motor maintains a steady operation at 347 rpm under a load torque of 40 mNm. During this time, the PPC current ranges from 370 mA to 800 mA, and the voltage ranges from 5 V to 6.1 V, and the HPLD current ranges from 2.37 A to 2.6 A. At around 6 seconds, a command is issued to reset the speed reference to 0 rpm. This causes a rapid drop in both current and voltage, with the current falling to about 460 mA and the voltage dropping to around 0.65 V within 2 seconds, leading to the motor coming to a stop. At around 14 s, a command is given to restore the speed reference to 347 rpm, prompting the motor to restart. The current quickly rises to around 630 mA, fluctuates between 570 mA and 680 mA, and then stabilizes in the range of 465–760 mA. Similarly, the voltage eventually stabilizes around 6 V. The motor takes about 2 seconds to reach the desired speed after starting up. See Supplementary Movie 1 for the details. It is worth mentioning that both current and voltage exhibit minimal ripple when the motor stops, demonstrating the rejection of output ripple in the photonic converter. The current and voltage ripples observed when the motor rotates, are caused by the commutation of the DC motor's commutator[4].

Test situation 2: following a sinusoidal speed reference with constant load. Figure 7a, b presents the experimental results for the second test situation, focusing on the response to a sinusoidally varying speed reference command. In this experiment, the speed reference command exhibits a sinusoidal waveform with a frequency of 0.05 Hz and an amplitude of 30 rpm, which is superimposed on the constant speed of 347 rpm, under a load torque of 40 mNm. A more

https://doi.org/10.1038/s41467-024-53924-9

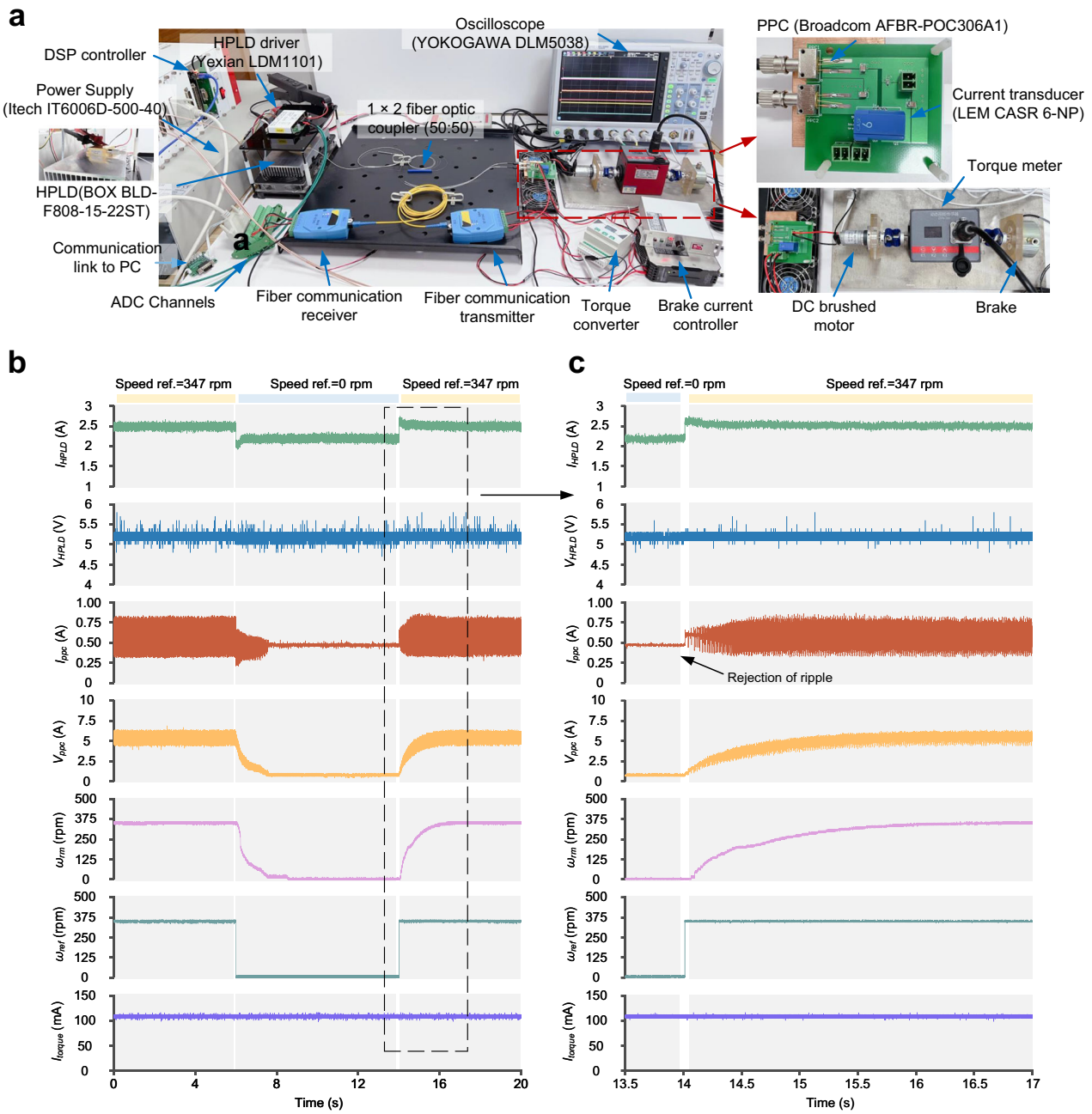

Fig. 6 | Experimental results of speed control for the photon-driven DC motor system. a Photograph of the experimental setup. **b**,**c** The system's performance during both halt and initiation phases with rejection of ripple. Initially, the brushed DC motor maintains a constant speed of 347 rpm under a load torque of 40 mNm. At about 6 s, the speed command is adjusted to 0 rpm, and then back to 347 rpm at about 14 s; global picture (**b**) and local picture (**c**).

detailed view of the sinusoidal variation is provided in Fig. 7a, b, showing one cycle of the waveform. Within one cycle, the range of PPCs current changes from a range of 0.395–0.760 A to a range of 0.440–0.760 A. The voltage demonstrates a variation range from a range of 4.6–5.6 V to a range of 5.4–6.4 V. The experimental results indicate that the speed control system effectively tracks the sinusoidally varying speed reference command. See Supplementary Movie 2 for the details.

Test situation 3: tracking constant speed with load disturbance. Figure 7c, d presents the experimental results for the third test condition, which explores the response of the proposed system under varying load torque conditions. Initially set at 347 rpm with a 40 mNm load, the motor experiences a sudden shift to no-load conditions at 15 s. The abrupt change causes an excess of electromagnetic torque, which leads to an unintended speed increase. To counteract the situation, the system dynamically adjusts the PPC current, reducing electromagnetic torque and moderating the current from a range of 0.38–0.8 A down to a range of 0.03–0.32 A. This action mitigates the speed increase, stabilizing it back to 347 rpm at about 22 s. The reapplication of the 40 mNm load torque at about 35 s further tests the system's resilience. This increase in load torque causes an immediate rise in current and a drop in voltage, reflecting the motor's struggle against the increase in load torque. Then, the speed control promptly elevates the PPC current, boosting electromagnetic torque to counter the impact of increasing load torque. The voltage, after initially falling, starts to climb, showing a recovery in motor speed. By about 40 s, motor operation normalizes, returning the initial parameters with a

https://doi.org/10.1038/s41467-024-53924-9

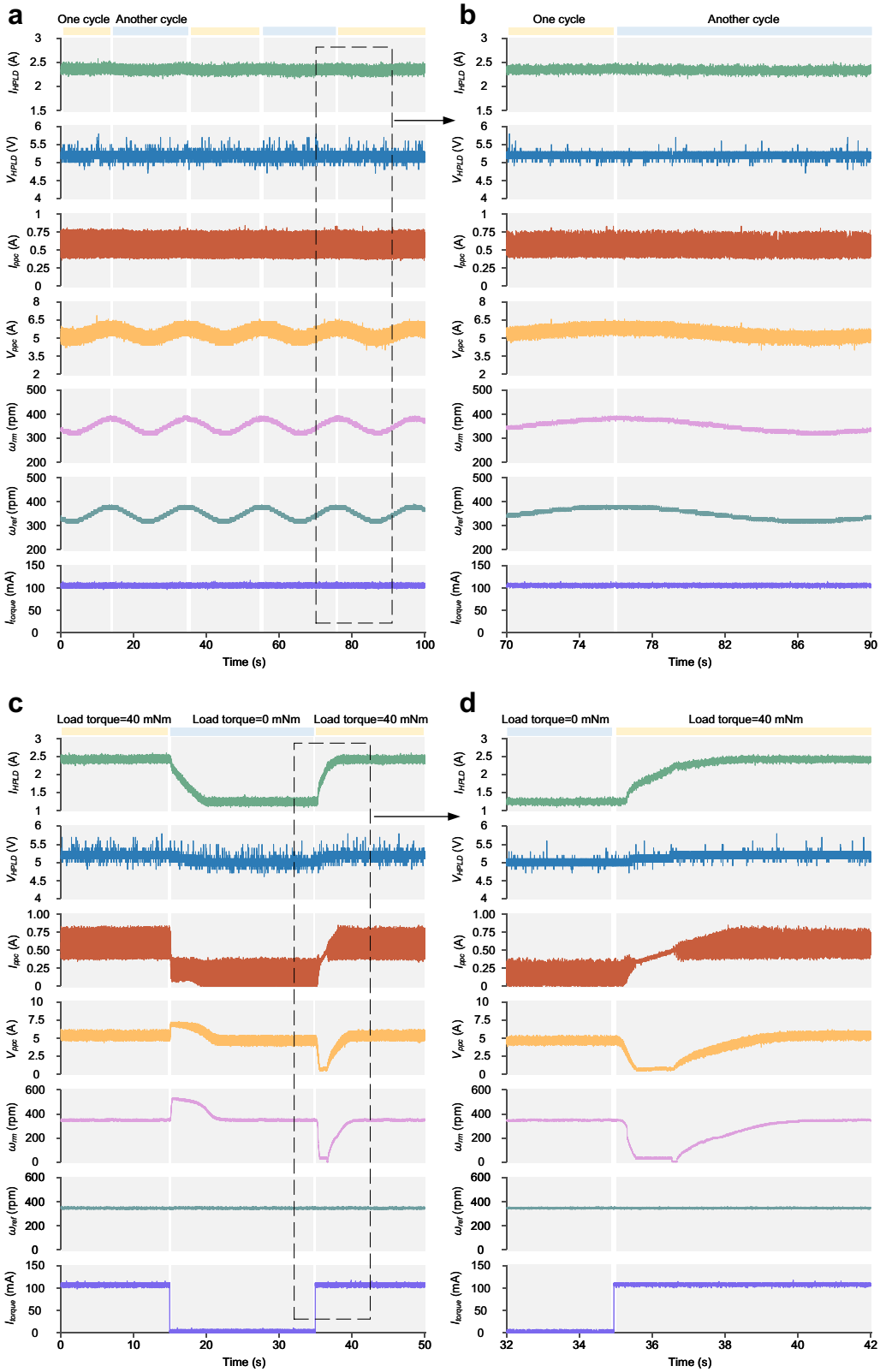

Fig. 7 | Experimental results of speed control for the photon-driven DC motor system. The system's capability to track a sinusoidal speed setpoint with a 0.05 Hz frequency under a constant load torque of 40 mNm; global picture (**a**) and local picture (**b**). The system's response to variations in load torque; starting from a base speed of 347 rpm with a 40 mNm load, the torque is reduced to 0 mNm at about 15 s, and subsequently restored to 40 mNm at about 35 s; global picture (**c**) and local picture (**d**).

https://doi.org/10.1038/s41467-024-53924-9

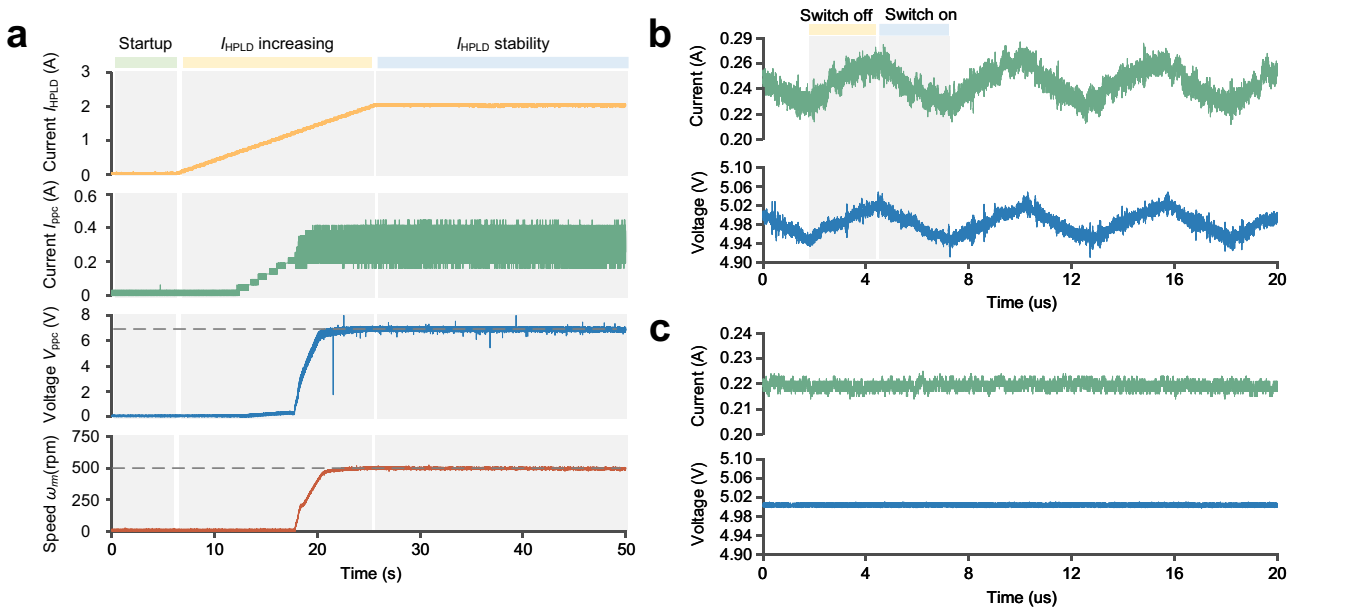

Fig. 8 | Model validation experiment and comparison of output ripple between switching electricity converter and photonic converter. a Under a 20 mNm load torque, motor speed, voltage, and current responses to increasing HPLD injection current from 0 A to 2 A starting at 6.3 s and continuing until 25.6 s, over 19.3 s. Notably, at 22.4 s, the motor reached its speed limit at ~500 rpm, while PPC voltage peaked between 6.77 V and 7.09 V, demonstrating a speed limit. **b** Output ripple of the switching electricity converter with a load resistance of 20 Ω. **c** Output ripple of the photonic converter with the load resistance of 20 Ω.

voltage range of 4.8–6 V and maintaining the set speed of 347 rpm. This experiment shows that the speed control is effective in keeping the motor speed steady, even when the load torque changes. It demonstrates the system's robustness in real-time adjustments. See Supplementary Movie 3 for the details.

Experimental verification of speed limit and output ripple

Figure 8a illustrates an experiment conducted to confirm the presence of a speed limit as shown in the model. The motor, operating under open-loop control with a 20 mNm load torque, shows variations in speed, voltage, and current with increasing HPLD injection current from 0 A to 2 A, starting at 6.3 s and continuing until 25.6 s. Initially, the low PPC voltage indicated the motor is stationary. Once rotation starts, the PPC voltage surges. At about 22.4 s, the motor's speed stabilizes at approximately 500 rpm, and the PPC voltage stabilizes between the range from 6.77 V to 7.09 V, slightly below the PPC's open-circuit voltage of 7.2 V, despite further increases in HPLD current. This experimental result confirms the speed limit of the above discussion, demonstrating the motor's speed stabilization despite increasing HPLD current.

To compare the output ripple between the photonic converter and the switching electricity converter, experimental comparisons were conducted. Both converters carry a load resistance of 20 Ω and have an output voltage of 5 V and an output current of 0.25 A. Figure 8b, c show the output voltage and output current of the switching electricity converter and the output voltage and output current of the photonic converter, respectively. The output ripple in the switching electricity converter can be observed due to its on-off switching actions. In the photonic converter, the output ripple is almost non-existent, and the voltage and current are almost a straight line.

Experimental verification of intrinsic EMI of proposed system

The intrinsic EMI of the proposed system and conventional system is measured by assessing the intensity of electromagnetic field emission from both. A YOKOGAWA DLM5038 oscilloscope (2.5 GS/s) is utilized for monitoring voltage and current variations, and an H field probe is used to monitor the intensity of electromagnetic field emission.

Figure 9 shows the EMI measurement experimental results of photon-driven DC motor system with load torque (40 mNm) and sinusoidal speed reference (superimpose a sine speed command with an amplitude of 30 rpm on a speed of 347 rpm). Figure 9a shows the close-up photo of setup. The H field probe is positioned approximately 2 cm directly above the photonic converter, as shown in Fig. 9a. Figure 9b, c show the oscilloscope wave of experiment results, including the HPLD voltage, HPLD current, PPCs voltage, PPCs current, speed, reference speed, torque-current, and the output voltage of the H field probe. Figure 9d shows the voltage ripple measured from the H field probe. Based on Fig. 9d, Fig. 9e shows the intensity of the intrinsic EMI. In Fig. 9e, the red line represents the intensity of electromagnetic field emissions when the proposed system is powered off, and the blue line represents the intensity of electromagnetic field emissions when the proposed system is powered on. From Fig. 9e, it can be observed that the blue line is very close to the red line with little difference, which indicates that the proposed system emits little electromagnetic field emissions.

Figure 10 shows the EMI measurement experimental results of conventional switching electricity converter-driven DC motor system with load torque (40 mNm) and sinusoidal speed reference (superimpose a sine speed command with an amplitude of 30 rpm on a speed of 347 rpm). Figure 10a shows the close-up photo of setup. The H field probe is positioned ~2 cm directly above the switching power converter, as shown in Fig. 10a. Figure 10b, c show the oscilloscope wave of experiment results, including motor voltage, motor current, speed, reference speed, torque current, and the output voltage of the H field probe. Based on Fig. 10d, e shows the intensity of the intrinsic EMI. In Fig. 10e, the red line represents the intensity of electromagnetic field emissions when the conventional system is powered off, and the blue line represents the intensity of electromagnetic field emissions when the conventional system is powered on. It can be seen that the blue line is obviously greater than the red line, which indicates that conventional systems emit much electromagnetic field emissions. From Fig. 9e, 10e, it can be observed that the proposed system reduces EMI compared to the conventional system. Experimental verification of intrinsic EMI of photonic converter is shown in the Supplementary Note 4. See Supplementary Movie 4 for the details.

https://doi.org/10.1038/s41467-024-53924-9

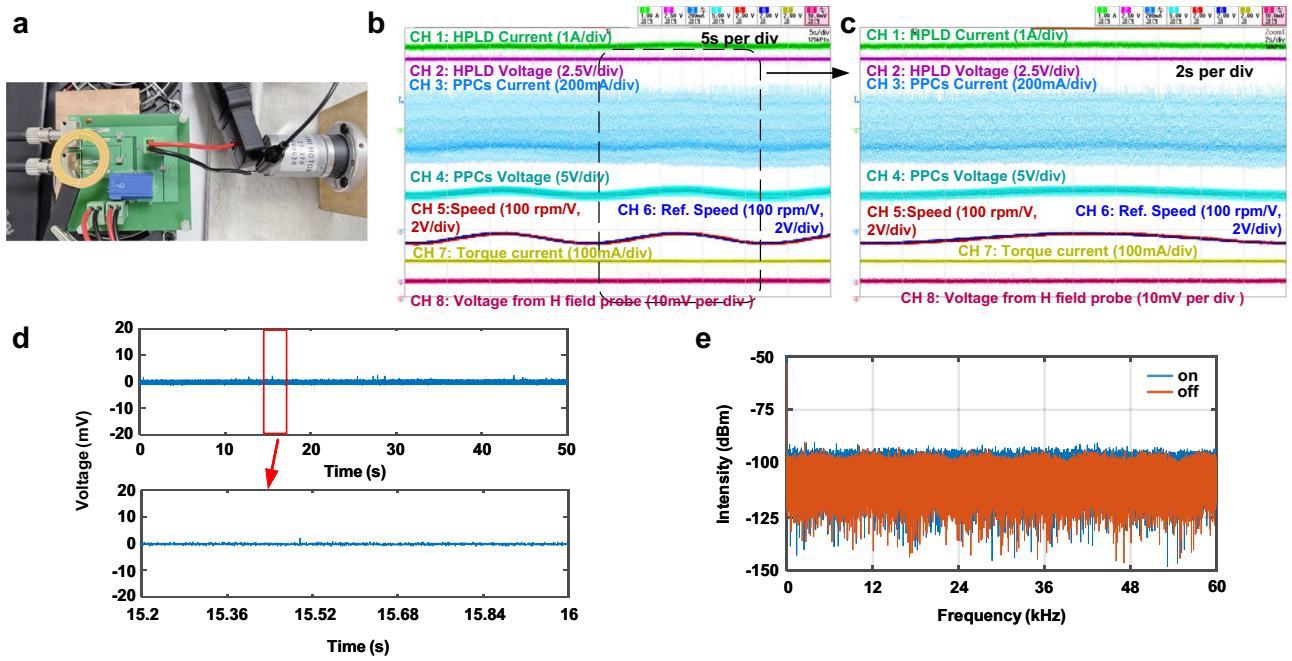

Fig. 9 | EMI measurement experiment results of proposed system with motor under load torque and sinusoidal speed reference. a Close-up photo of the photonic converter and motor under test. Oscilloscope waveform of experiment results; global picture (**b**) and local picture (**c**). **d** Output voltage waveforms from the H field probe. **e** Intensity of the intrinsic EMI, measured when proposed system is powered on (in blue) and off (in red).

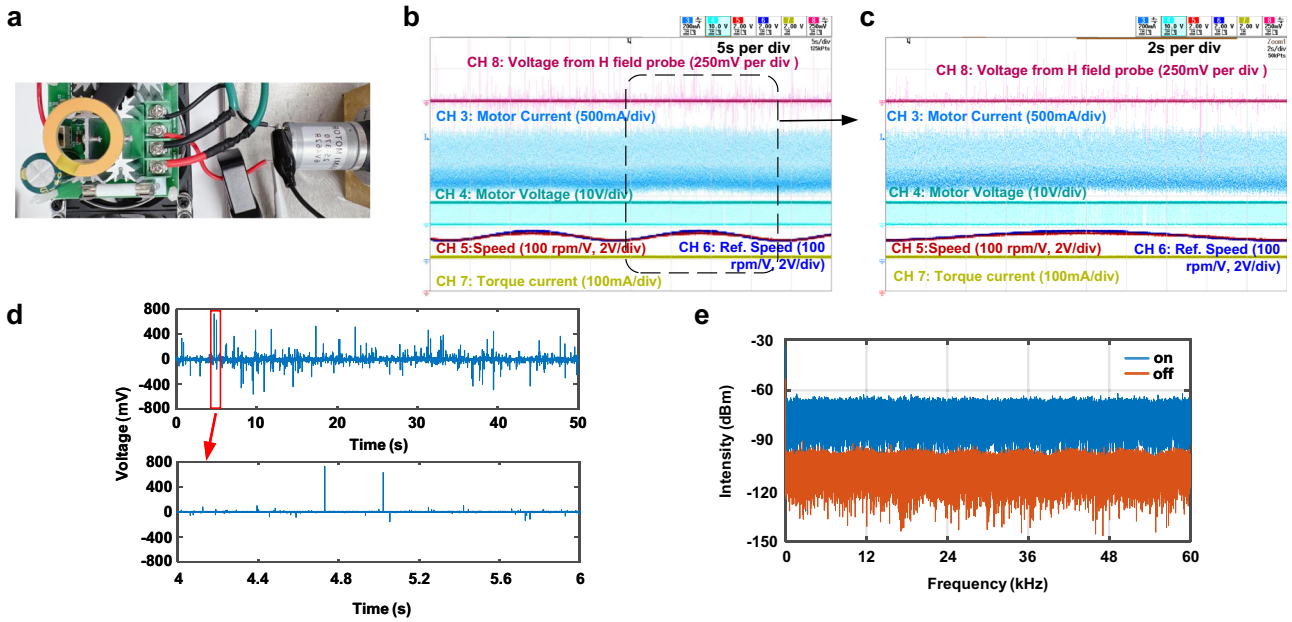

Fig. 10 | EMI measurement experiment results of conventional system with motor under load torque and sinusoidal speed reference. a Close-up photo of the switching power converter and motor under test. Oscilloscope waveform of experiment results; global picture (**b**) and local picture (**c**). **d** Output voltage waveforms from the H field probe. **e** Intensity of the intrinsic EMI, measured when conventional system is powered on (in blue) and off (in red).

Discussion

In this study, a photon-driven DC motor system is proposed, including its HPLD-PPC-Motor model, operation principle, and PM-based speed control. In this system, a HPLD converts electrical energy into optical energy, which is transmitted via optical fibers to photovoltaic power converters, transforming it back into electrical energy to drive motor. Unlike conventional switching converter-driven DC motor systems, which rely on the rapid on-off switching actions in switching electricity converters, the proposed system utilizes a photonic converter to drive the DC motor without switching actions. Hence, the proposed system not only eliminates the intrinsic EMI and output ripple generated by the rapid on-off switching actions in switching electricity converters, but also utilizes the non-conductive nature of optical fibers for immunity to environmental EMI.

To validate the proposed system, an experimental prototype was constructed, and experimental verifications of PM-based speed control were conducted in three situations. These experiments demonstrated the system's capability to effectively track reference speeds

and preserve motor speed consistency amidst varying load torques. The speed limit of the motor, as shown in the theoretical model analysis, was also verified. Experiments compare the electromagnetic field emission and output ripple between the commercial switching electricity converter and the photonic converter.

The proposed photon-driven DC motor system offers a promising alternative solution for motor control, especially in industries requiring electromagnetic compatibility. The proposed system is possible to apply in the following application scenarios: (1) mobile tethered unmanned aerial vehicle (tUAV) for monitoring high voltage transmission lines (see Method for the advantages of the tUAV); (2) auxiliary motor drive system of electromagnetic catapult system, which can be used in space launch, missile defense, high-pressure research, aircraft catapult. Future research should concentrate on enhancing the energy conversion efficiency and expanding the applicability of the photonic converter in diverse and challenging environments. Besides, the proposed photon-driven DC motor system requires the PPC, and the PPC is not cheap because it is not currently used on a large scale in industry.

Methods

HPLD model

The HPLD driver controls the injection current of the HPLD I_{HPLD} depending on the control signal generated by the controller, as shown in Fig. 3a. The power of the high-power light P_{light_HPLD} of the HPLD increases linearly with the I_{HPLD}[35,36], according to

$$P_{light\,HPLD} = R_{HPLD}\left(I_{HPLD} - I_{th}\right) \tag{3}$$

where R_{HPLD} is the differential slope efficiency, which can be considered as a constant parameter; I_{th} is the threshold current of the HPLD. In this study, a commercial HPLD (BOX Company Ltd. BLD-F808-15-22ST) is used to provide up to 15 W of optical power output, which is launched into the 0.5 m MMFs (105/125 µm, NA 0.22) at nominally 808 nm wavelength. Considering the influence of temperature, temperature control is critical in maintaining the stability of HPLD output characteristics. Power–current curve and voltage–current curve of the HPLD under a temperature range from 20 °C to 40 °C are shown in Supplementary Fig. 7. For this purpose, passive air-cooled heat sinks are utilized to stabilize the HPLD temperature at the ambient room temperature.

Fiber model

The high-power light generated from the HPLD is transmitted by the optical fiber and then illuminated to the PPC. There is power loss in the propagation of light in optical fibers. Bouguer-Beer–Lambert law[37] is used to calculate the power loss and power efficiency of optical energy transmission in fiber, which shows that the power of light attenuates exponentially with distance due to the material's properties, like absorption and scattering in the fiber. This attenuation, measured as the attenuation coefficient α in decibels per kilometer (dB/km), depends on the distance of light propagation and its wavelength.

According to Bouguer-Beer–Lambert law[37], for a transmission distance of z km, the attenuation of the high-power light is αz dB. Thus, the power efficiency of the high-power light η_{trans} can be expressed as[38]

$$\eta_{trans} = \frac{P_{light\,PPC}}{P_{light\,HPLD}} = e^{-\alpha z/10} \tag{4}$$

where P_{light_PPC} is the input optical power of PPC, and P_{light_HPLD} is the output optical power of HPLD. The power loss P_{loss} can be expressed as $P_{loss} = P_{light\_HPLD}(1 - \eta_{trans})$.

PPC model

The widely used PPC model is the single diode model due to its tradeoff between accuracy and simplicity. In the single diode model[44,45], main parameters include current flowing I_{ppc}, voltage across the PPC V_{ppc}, photogenerated current I_{ph}, diode reverse saturation current I_o, series resistance R_s, and shunt resistance R_{sh}, as shown in Fig. 3a. The I_{ppc} is represented by

$$I_{ppc} = I_{ph} - I_o\left[\exp\left(\frac{V_{ppc} + I_{ppc}R_s}{nV_T}\right) - 1\right] - \frac{V_{ppc} + I_{ppc}R_s}{R_{sh}} \tag{5}$$

with

$$I_{ph} = R_{PPC}P_{light\,PPC} \tag{6}$$

where V_T is the junction thermal voltage and can be expressed as $V_T = kT/q$, and the k is the Boltzmann's constant equal to $1.3806 \times 10^{-23} J/K$; T is the absolute temperature; $q = 1.6022 \times 10^{-19} C$ is the electron charge; n is the diode ideality constant; R_{PPC} is differential responsivity, which can generally be considered as a constant. P_{light_PPC} is the input optical power irradiated on the PPC photosensitive surface. In Eq. (5), R_{sh}, n, I_o, and R_s are four unknown parameters. These parameters depend on the material and manufacturing process of the PPC, which can be calculated by measuring other parameters of the PPC under rated optical power.

To ascertain the four unknown parameters, a comprehensive analysis of the PPC current–voltage (I–V) characteristics is conducted. These parameters are deduced from the short-circuit current I_{sc}, open-circuit voltage V_{oc}, output current at the maximum power point I_m, and the corresponding output voltage V_m. Besides, the slopes at the open-circuit point R_{so} and the short-circuit point R_{sho} are derived from the I–V curve. Under short-circuit conditions, the output terminals of the PPC are connected in a closed loop, resulting in the highest possible current flow, which corresponds to the I_{sc}. Conversely, when the output terminals are open, the voltage across the PPC reaches its peak, equaling the V_{oc}. During operation at the maximum power point, the output current matches the I_m, and the voltage across the PPC is identified as the V_m. To precisely determine the values of R_{sho} and R_{so}, a linear fit is applied to the current and voltage data in the vicinity of the short-circuit current and open-circuit voltage points, respectively. The R_{sh} is equal to the R_{sho}, Thus R_{sho} and R_{so} can be expressed by

$$R_{sho} = R_{sh} = -\left(\frac{dV}{dI}\right)_{I=Isc} \tag{7}$$

with

$$R_{so} = -\left(\frac{dV}{dI}\right)_{V=Voc} \tag{8}$$

The diode ideality constant of the diode can be calculated by

$$n = \frac{A_{part}}{V_t\left(B_{part} + C_{part}\right)} \tag{9}$$

with

$$A_{part} = V_m + R_{so}I_m - V_{oc} \tag{10}$$

$$B_{part} = \ln\left(I_{sc} - \frac{V_m}{R_{sh}} - I_m\right) - \ln\left(I_{sc} - \frac{V_{oc}}{R_{sh}}\right) \tag{11}$$

$$C_{part} = \frac{I_m}{I_{sc} - \frac{V_{oc}}{R_{sh}}} \tag{12}$$

The other parameters I_o, R_s are obtained using the following equations as

$$I_o = \left(I_{sc} - \frac{V_{oc}}{R_{sh}}\right) \exp\left(-\frac{V_{oc}}{nV_T}\right) \tag{13}$$

$$R_s = R_{so} - \frac{nV_t}{I_o} \exp\left(-\frac{V_{oc}}{nV_T}\right) \tag{14}$$

The vertical multi-junction GaAs-based PPC (Broadcom AFBR-POC306A1) is used in this work, as shown in Fig. 3e. Using the Eqs. (7)–(14), the parameters of AFBR-POC306A1 are shown in Supplementary Table 2 and Supplementary Table 3. Similar to the HPLD, the temperature affects the characteristics of the PPC. Thus, the passive air-cooled heat sinks are also utilized to stabilize the PPC temperature at the ambient room temperature. Supplementary Fig. 8 shows the short-circuit current and maximum power point current of the PPC as a function of case temperature at 808 nm.

Brushed DC motor model

The equivalent circuit model of the brushed DC motor is shown in Fig. 3a. Under the assumption that the armature reaction is perfectly canceled out by the commutating poles and the compensation winding, the brushed DC motor can be modeled using the following equations by ref.[1]

$$V_{ppc} = R_a I_a + L_a \frac{dI_a}{dt} + K_e w_{rm} \tag{15}$$

with

$$e = K_e w_{rm} \tag{16}$$

where V_{ppc} is the terminal voltage of the brushed DC motor, R_a is the equivalent armature winding resistance, I_a is the armature current, L_a is the equivalent armature winding inductance in H, e is the back EMF, K_e presents the back EMF constant, ω_{rm} is the speed rotor.

The equation of the motion of the rotor can be expressed by

$$T_e = J\frac{dw_{rm}}{dt} + Bw_{rm} + T_L \tag{17}$$

with

$$T_e = K_t I_a \tag{18}$$

where T_e is the electromagnetic torque of the DC motor, J is the total inertia of the rotating part, B is the viscous damping coefficient, T_L is the load torque, K_t is the torque constant. In the steady state, the rotating speed of the DC motor is constant as $d\omega_{rm}/dt = O$, and the armature current is also constant as $dI_a/dt = O$. Thus, the torque of the DC motor is equal to the load torque and friction torque ($T_e = B\omega_{rm} + T_L$). The I–V curve, e–ω_{rm} curve, and T_e–I_a curve of the brushed DC motor used in this study are shown in Supplementary Figs. 9a, 9b, and 9c, respectively. The parameters of this brushed DC motor are listed in Supplementary Table 4.

Function derivation on HPLD-PPC-motor model

HPLD-PPC-Motor model is composed of HPLD model, fiber model, PPC model, and motor model (See Supplementary Fig. 10 for detailed derivation process). By integrating Eqs. (3), (4), and (6), the I_{ph} as a function of I_{HPLD} is expressed as

$$I_{ph} = R_{HPLD}\eta_{trans}R_{PPC}(I_{HPLD} - I_{th}) \tag{19}$$

where R_{HPLD}, η_{trans}, R_{PPC}, and I_{th} can be considered as constant, thus $I_{ph} \propto I_{HPLD}$ in the linear interval of the HPLD. $I_{ppc} = I_a + I_c$, due to the parallel connection between PPC and DC motor in HPLD-PPC-Motor model as shown in Fig. 2a. Based on Eq. (15), the V_{ppc} can be expressed as

$$V_{ppc} = \left(I_{ppc} - I_c\right)R_a + L_a\frac{d\left(I_{ppc} - I_c\right)}{dt} + K_e\omega_{rm} \tag{20}$$

By integrating Eqs. (5) and (19), the I_{ppc} can be expressed as

$$I_{ppc} = R_{HPLD}\eta_{trans}R_{PPC}(I_{HPLD} - I_{th}) - I_o\left[\exp\left(\frac{V_{ppc} + I_{ppc}R_s}{nV_T}\right) - 1\right] - \frac{V_{ppc} + I_{ppc}R_s}{R_{sh}} \tag{21}$$

Based on Eq. (17), the ω_{rm} can be expressed as

$$\omega_{rm} = \frac{K_t\left(I_{ppc} - I_c\right) - T_L - J(d\omega_{rm}/dt)}{B} \tag{22}$$

By integrating Eqs. (20)–(22), the ω_{rm} as a function of I_{HPLD} and T_L can be written as

$$\omega_{rm} = \frac{K_t}{B}\left[R_{HPLD}\eta_{trans}R_{PPC}(I_{HPLD} - I_{th})\right] - \frac{K_tI_o}{B}\left[\exp\left(\frac{A_1}{nV_T}\right) - 1\right] - \frac{K_tA_1}{BR_{sh}} - \frac{K_tI_c}{B} - \frac{T_L}{B} - \frac{J}{B}\frac{d\omega_{rm}}{dt} \tag{23}$$

with

$$A_1 = \frac{B\omega_{rm} + T_L + J\frac{d\omega_{rm}}{dt}}{K_t}R_a + K_e\omega_{rm} + \left(\frac{B\omega_{rm} + T_L + J\frac{d\omega_{rm}}{dt}}{K_t} + I_c\right)R_s + L_a\frac{d\left(B\omega_{rm} + T_L + J\frac{d\omega_{rm}}{dt}\right)}{dt} \tag{24}$$

From Eqs. (23) and (24), it can be observed that T_L is an environmental variable which affect the ω_{rm}, while the ω_{rm} can be controlled by the I_{HPLD}. Factors of the transient state are considered, such as speed variance and inductance voltage, alongside the charging and discharging dynamics of capacitors. In a steady state, the ω_{rm} is constant as $d\omega_{rm}/dt = 0$, the I_a is also constant as $d(I_{ppc} - I_c)/dt = 0$, and capacitor voltage is constant as $I_c = O$. Thus, the ω_{rm} at the steady state is the function of I_{HPLD} and T_L as

$$\omega_{rm} = \frac{K_t}{B}\left\{\left[R_{HPLD}\eta_{trans}R_{PPC}(I_{HPLD} - I_{th})\right] - I_o\left[\exp\left(\frac{A_2}{nV_T}\right) - 1\right]\right\} - \frac{K_tA_2}{BR_{sh}} - \frac{T_L}{B} \tag{25}$$

with

$$A_2 = \frac{B\omega_{rm} + T_L}{K_t}R_a + K_e\omega_{rm} + \frac{B\omega_{rm} + T_L}{K_t}R_s \tag{26}$$

where a desired ω_{rm} is regulated by I_{HPLD} to accommodate the environmental T_L variations.

Experimental setup

In the experimental prototype for the photonic converter, illustrated in Fig. 6a, a HPLD driven by a Yexian LDM1101 is deployed, powered by a DC source (Itech IT6006D-500-40). This setup is controlled

through a digital signal processor (DSP) incorporating an integrated speed control, with RS485 communication enabling real-time monitoring of operational parameters on a computer. Supplementary Table 5 shows controller parameters for experimental verification of PM-based speed control. The high-power light with a wavelength of 808 nm generated by the HPLD (BOX BLD-F808-15-22ST) is coupled into a multimode fiber (MMF105/125 NA0.22), where the rated output optical power is 15 W. The PPC (Broadcom AFBR-POC306A1) has a maximum input optical power of 6 W and a rated output electrical power of 3 W. The chosen HPLD can power two chosen PPCs simultaneously since its rated output power is over double the rated input power of a single PPC. To achieve that one HPLD powers two PPCs, the fiber coupler is used, which can split the input power from the HPLD and allocate the output power to two PPCs according to a certain proportion. In this study, the 1×2 fiber coupler (50:50) is used (MC Fiber Optics MMFBTC026), which can allocate input power to two output fibers in a ratio of 50 to 50. (See Supplementary Note 5 for the principle of fiber coupler in photonic converter and the parameters of fiber coupler are listed in Supplementary Table 6).

This arrangement, with two PPCs connected in parallel to both the motor and several ceramic capacitors with a capacitance of 660uF, ensures enhanced voltage stability. In the printed circuit board of the PPC, the current transducer (LEM CASR 6-NP) is used to measure the current. The brushed DC motor chosen for this work is a stator bipolar with a three-slot rotor. This motor is equipped with a reduction gearbox with a reduction ratio of 1:13 to achieve greater torque and facilitate experimental testing. The desired load torque is generated by the brake (HAIBOHUA HB-02M-0.2Nm), which is controlled by the intelligent brake current controller (HAIBOHUA CSM-500), by adjusting the injection current of the brake to control load torque. The speed sensor, an incremental encoder in the torque meter is utilized within the experimental setup for measuring the real-time speed of the brushed DC motor. Through fiber communication transmitter and receiver, the real-time feedback signals obtained from sensors are converted into optical signals for communication achieving immunity EMI. The analog-to-digital converter channels of the DSP controller adopt the real-time signal from the fiber communication receiver for the speed control. The HPLD current, HPLD voltage, PPCs current, the terminal voltage of the motor, speed of the motor, reference speed and output current from the intelligent brake current controller, are visualized by an oscilloscope (YOKOGAWA DLM5038).

Advantages of tUAV

Tethered UAVs (tUAVs) offer several advantages over untethered UAVs (uUAVs) due to their continuous power supply and secure data transmission capabilities, as follows.

Continuous Power Supply and Extended Flight Times: tUAVs are connected to a ground-based power source (ground station) through a cable, which provides them with a continuous power supply. This eliminates the need for onboard batteries and allows them to remain airborne for extended periods. This is particularly beneficial for tasks that require long-term monitoring or continuous operation, where battery life would otherwise limit the duration of flight.

Stable Data Transmission: The tether cable used in tUAVs not only supplies power but can also be used for data transmission. This setup ensures a stable and reliable communication link between the UAV and the ground station, reducing the risks of data loss and delays that are common with wireless communications. The direct physical connection provides higher data transfer rates and greater security against interception or interference.

Increased Payload Capacity: Some tUAVs are designed to carry heavier payloads because they do not need to carry their power source (batteries). This capability allows them to equip more substantial or multiple pieces of equipment, making them ideal for specialized tasks that require significant on-board technology.

Reduced Risk: The tethered design minimizes the risk of UAVs getting lost or flying beyond the operator's control range. This is especially useful in complex or confined environments, where maintaining control of the uUAV could be challenging.

Data availability

Source data are provided with this paper.

Code availability

The code to implement the DSP control for experimental verification of PM-based speed control is available at the supplementary document.

References

1. Sul, S. K. *Control of Electric Machine Drive Systems* (Wiley, 2011).
2. Wang, S., Hong, J., Sun, Y. & Cao, H. Effect comparison of zigzag skew PM pole and straight skew slot for vibration mitigation of PM brush DC motors. *IEEE Trans. Ind. Electron.* **67**, 4752–4761 (2020).
3. Scott, JH., McLeish, J. & Round, W. Speed Control with Low Armature Loss for Very Small Sensorless Brushed DC Motors. *IEEE Trans. Ind. Electron.* **50**, 1682–1687 (2009).
4. Sánchez, E. S., Gil, J. G., Real, J. C. G. & Higuera, J. F. D. A new method for sensorless estimation of the speed and position in brushed DC motors using support vector machines. *IEEE Trans. Ind. Electron.* **59**, 1397–1408 (2012).
5. Kahoul, R., Azzouz, Y., Ravelo, B. & Mazari, B. New behavioral modeling of EMI for DC motors applied to EMC characterization. *IEEE Trans. Ind. Electron.* **60**, 5482–5496 (2013).
6. Malaric, K. *EMI Protection for Communication Systems* (Artech House, 2010).
7. Bendicks, A., Dörlemann, T., Osterburg, T. & Frei, S. Active cancellation of periodic EMI of power electronic systems by injecting artificially synthesized signals. *IEEE Electromagn. Compat. Mag.* **9**, 63–72 (2020).
8. Sun, B., Burgos, R. & Boroyevich, D. Common-mode EMI unterminated behavioral model of wide-bandgap-based power converters operating at high switching frequency. *IEEE Trans. Emerg. Sel. Top. Power Electron.* **7**, 2561–2570 (2019).
9. Redouté, J. & Steyaert, M. Kuijk bandgap voltage reference with high immunity to EMI. *IEEE Trans. Circuits Syst. II Express Briefs* **57**, 75–79 (2010).
10. Wilkins, M. M. et al. Ripple-free boost-mode power supply using photonic power conversion. *IEEE Trans. Power Electron.* **34**, 1054–1064 (2019).
11. Barkas, D. A., Ioannidis, G. C., Psomopoulos, C. S., Kaminaris, S. D. & Vokas, G. A. Brushed DC motor drives for industrial and automobile applications with emphasis on control techniques: a comprehensive review. *Electronics* **9**, 887 (2020).
12. Degano, M., Zanchetta, P., Empringham, L., Lavopa, E. & Clare, J. HF induction motor modeling using automated experimental impedance measurement matching. *IEEE Trans. Ind. Electron.* **59**, 3789–3796 (2012).
13. Huangfu, Y., Wang, S., Rienzo, L. D. & Zhu, J. Radiated EMI modeling and performance analysis of a PWM PMSM drive system based on field-circuit coupled FEM. *IEEE Trans. Magn.* **53**, 1–4 (2017).
14. Huangfu, Y. et al. Conducted EMI simulation for a high power Ultra-precision PMSM driven by PWM converter. In *Proc. IEEE International Symposium on Electromagnetic Compatibility*, 645–650 (IEEE, 2016).
15. Nia, M. S. S., Shamsi, P. & Ferdowsi, M. EMC modeling and conducted EMI analysis for a pulsed power generator system including

an AC–DC–DC power supply. *IEEE Trans. Plasma Sci.* **48**, 4250–4261 (2020).
16. Nia, M. S. S., Shamsi, P. & Ferdowsi, M. EMC improvement for high voltage pulse transformers by pareto-optimal design of geometry structure based on parasitic analysis and EMI propagation. *CSEE J. Power Energy Syst.* **7**, 1051–1063 (2021).
17. Stefanie, H., Jacobs, K., Ilves, K., Norrga, S. & Nee, H. Auxiliary power supplies for high-power converter submodules: state of the art and future prospects. *IEEE Trans. Power Electron.* **37**, 6807–6820 (2022).
18. Zhao, B., Assawaworrarit, S., Santhanam, P., Orenstein, M. & Fan, S. High-performance photonic transformers for DC voltage conversion. *Nat. Commun.* **12**, 4684 (2021).
19. Matsuura, M., Tajima, N., Nomoto, H. & Kamiyama, D. 150-W power-over-fiber using double-clad fibers. *J. Light. Technol.* **38**, 401–408 (2020).
20. Matsuura, M. et al. Over 40-W electric power and optical data transmission using an optical Fiber. *IEEE Trans. Power Electron.* **36**, 4532–4539 (2021).
21. Worms, K. et al. Reliable and lightning-safe monitoring of wind turbine rotor blades using optically powered sensors. *Wind Energy* **20**, 345–360 (2014).
22. Zhang, X. et al. A gate drive with power over fiber-based isolated power supply and comprehensive protection functions for 15-kV SiC MOSFET. *IEEE Trans. Emerg. Sel. Top. Power Electron.* **4**, 946–955 (2016).
23. Budelmann, C. Opto-electronic sensor network powered over fiber for harsh industrial applications. *IEEE Trans. Ind. Electron.* **65**, 1170–1177 (2018).
24. Svetlana, V. B. et al. Roadmap on optical energy conversion. *J. Opt.* **18**, 073004 (2016).
25. Algora, C., et al. Beaming power: photovoltaic laser power converters for power-by-light. *Joule* **6**, 340–368 (2022).
26. Gou, Y. et al. High-performance laser power converts for direct-energy applications. *Opt. Express* **30**, 31509–31517 (2022).
27. Fafard, S. & Masson, DP. Perspective on photovoltaic optical power converters. *J. Appl. Phys.* **130**, 160901 (2021).
28. Fafard, S. et al. High-photovoltage GaAs vertical epitaxial monolithic heterostructures with 20 thin p/n junctions and a conversion efficiency of 60%. *Appl. Phys. Lett.* **109**, 131107 (2016).
29. Fafard, S. et al. Ultrahigh efficiencies in vertical epitaxial heterostructure architectures. *Appl. Phys. Lett.* **108**, 071101 (2016).
30. Emelyanov, V. M., Mintairov, S. A., Sorokina, S. V., Khvostikov, V. P. & Shvarts, M. Z. Simulation of the ohmic loss in photovoltaic laser-power converters for wavelengths of 809 and 1064 nm. *Semiconductors* **50**, 125–131 (2016).
31. Wagner, L. et al. Integrated series/parallel connection for photovoltaic laser power converters with optimized current matching. *Prog. Photovolt.* **29**, 172–180 (2020).
32. Kishk, M. A., Bader, A. & Alouini, M. Aerial base station deployment in 6 G cellular networks using tethered drones: the mobility and endurance tradeoff. *IEEE Veh. Technol. Mag.* **15**, 103–111 (2020).
33. Jain, K. P., Kotaru, P., Sa, M. D., Mueller, M. W., & Sreenath, K. Tethered power supply for quadcopters: architecture, analysis and experiments. *arXiv* https://arxiv.org/abs/2203.08180 (2022).
34. Jain, K. P., & Mueller, M. W. Flying batteries: In-flight battery switching to increase multirotor flight time. In *Proc. IEEE International Conference on Robotics and Automation (ICRA)*, 3510–3516 (IEEE,2019).
35. Mena, P. V., Morikuni, J. J., Kang, S. S., Harton, A. V. & Wyatt, K. W. A simple rate-equation-based thermal VCSEL model. *J. Light. Technol.* **17**, 865–872 (1999).
36. Zhou, W. & Jin, K. Efficiency evaluation of laser diode in different driving modes for wireless power transmission. *IEEE Trans. Power Electron.* **30**, 6237–6244 (2015).
37. Mayerhöfer, T. G., Pahlow, S. & Popp, J. The Bouguer-Beer-Lambert law: shining light on the obscure. *Chemphyschem* **21**, 2029–2046 (2020).
38. Bahaa, E. A. S. & Malvin C. T. *Fundamentals of Photonics* (Wiley, 2019).
39. Matsuura, M. Recent advancement in power-over-fiber technologies. *Photonics* **8**, 335 (2021).
40. Wang, B. et al. High reliability 808 nm laser diodes with output power over 19 W under CW operation. *IEEE Photon. Technol. Lett.* **34**, 349–352 (2022).
41. Crump, P. A. et al. 975 nm high power diode lasers with high efficiency and narrow vertical far field enabled by low index quantum barriers. *Appl. Phys. Lett.* **96**, 131110 (2010).
42. Helmers, H. et al. 68.9% efficient GaAs-based photonic power conversion enabled by photon recycling and optical resonance. *Phys. Status Solidi RRL* **15**, 2100113 (2021).
43. Yoshikawa, K. et al. Silicon heterojunction solar cell with interdigitated back contacts for a photoconversion efficiency over 26%. *Nat. Energy* **2**, 17032 (2017).
44. Cotfas, D. T., Cotfas, P. A. & Kaplanis, S. Methods to determine the dc parameters of solar cells: a critical review. *Renew. Sust. Energ. Rev.* **28**, 588–596 (2013).
45. Shongwe, S. & Hanif, M. Comparative analysis of different single-diode pv modeling methods. *IEEE J. Photovolt.* **5**, 938–946 (2015).

Acknowledgements

This work is supported by the National Natural Science Foundation of China (52277173, F. D.).

Author contributions

D.L. and F.D. conceived the idea, conducted the theoretical analysis, conducted experiments, and wrote the paper. W.H., M.C., Z.C., and Z.W. provided suggestions and comments and helped to organize and revise the manuscript. All authors discussed the results and contributed to the manuscript.

Competing interests

The authors declare no competing interests.

Additional information

Supplementary information The online version contains supplementary material available at https://doi.org/10.1038/s41467-024-53924-9.

Correspondence and requests for materials should be addressed to Fujin Deng.

Peer review information *Nature Communications* thanks Alberto Martinez-Barboa and the other, anonymous, reviewer(s) for their contribution to the peer review of this work. A peer review file is available.